Device for inductive heating and focusing of laser produced plasma

J. R. Creel, T. Donnelly, and J. G. Lunney

View Online   Export Citation   CrossMark

ARTICLES YOU MAY BE INTERESTED IN

Nanopositioning Systems

Modular Motion Control

AFM and NSOM Instruments

Single Molecule Microscopes

MCL
MAD CITY LABS INC.
www.madcitylabs.com

AIP Publishing
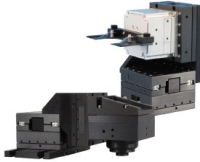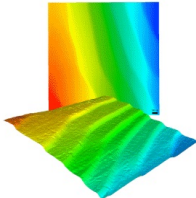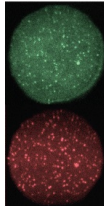
Review of Scientific Instruments

Device for inductive heating and focusing of laser produced plasma

View Online   Export Citation   CrossMark

J. R. Creel,[a] 🆔 T. Donnelly, 🆔 and J. G. Lunney 🆔

AFFILIATIONS

School of Physics, Trinity College Dublin, The University of Dublin, Dublin 2, Ireland

[a]Author to whom correspondence should be addressed: creelj@tcd.ie

ABSTRACT

The design and implementation of a pulsed magnetic induction device used to heat and focus a laser produced plasma in vacuum is described. Imaging of the plasma light emission and optical spectroscopy show that the UV/visible light emission is strongly enhanced, and the degree of ionization is increased. The plasma focusing is confirmed by contraction of the deposits formed by the plasma transmitted through the induction coil. The operation of the device can be described in the framework of resistive magnetohydrodynamics, where the induced currents heat the plasma and focus the plasma via the Lorentz interaction with the magnetic field.

Published under license by AIP Publishing. https://doi.org/10.1063/1.5108600

I. INTRODUCTION

Electric and magnetic fields have long been used to excite and manipulate plasmas, a technique which is useful in many areas, including magnetically confined fusion,[1] X-ray and EUV light sources for metrology,[2–4] and thin film deposition.[5,6] In particular, for pulsed laser deposition (PLD), magnetic control of the plasma gives enhanced deposition rates[7–9] and reduction of particulate contamination.[10] Previous work on magnetic effects in PLD mostly dealt with the expansion of the laser produced plasma (LPP) nearly parallel, or perpendicular, to a static magnetic field.[7,11–16] In regions where the plasma velocity u is not parallel to the magnetic field B, the $u \times B$ Lorentz interaction generates an electric field, which drives a current density j in the plasma. This current may heat the plasma, and the interaction of the current with B generates a body force, which accelerates the plasma. Mason and Goldberg[17,18] and Creel et al.[9,19] showed that using the magnetic induction associated with a pulsed magnetic field can lead to higher induced plasma currents and enhanced plasma heating, as compared to plasma flow across a static field. Creel et al.[9,19] also observed plume focusing through the interaction of the induced plasma current and the imposed magnetic field.

This paper provides a detailed description of the design and operation of the inductive heating device used in the experiments reported in Refs. 9 and 19. The influence of eddy currents in electrically conducting target was modeled and used to set the minimum separation between the induction coil and the target.

Plasma heating due to the induced current loop at the edge plasma was directly observed by head-on imaging of the enhanced plasma optical emission. The progress of this enhanced emission toward the plasma axis was interpreted in terms of magnetic field diffusion into the plasma. The strong enhancement of the plasma emission and increased ionization may be useful in laser induced breakdown spectroscopy (LIBS) in low pressure environments. The observation of plume focusing opens a new approach to control the deposition plume in PLD.

II. EXPERIMENTAL METHODS

A diagram of the experimental setup is shown in Fig. 1. It consists of a planar induction coil connected to an RLC circuit with a triggered switch. The whole setup was placed in a vacuum chamber at ~10^{-5} mbar. A 248 nm, 20 ns excimer laser beam is directed through the central aperture of the induction coil on to a copper target (99.95+% purity). The beam spot on the target was ~0.03 cm^{-2} giving a laser fluence of ~2 J cm^{-2}. Laser ablation produces a plasma plume expanding away from the target at ~16 mm μs^{-1}. An intensified charge coupled device (ICCD) camera was used to record images of the plume self-emission at various times after the laser pulse, with, and without excitation of the induction coil. Similarly, an ICCD camera connected to a spectrometer was used to record calibrated time- and space-resolved emission spectra. The ablated material was deposited on glass substrates placed at several
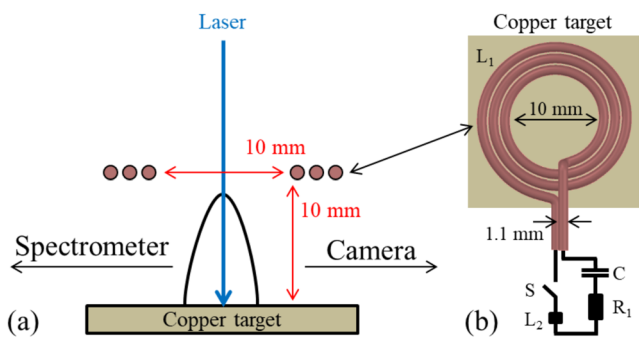
FIG. 1. (a) Side-on view of the experimental setup, and (b) face-on view of the target, induction coil, and driving circuit.

different distances from the target to reveal how the pulsed magnetic field leads to focusing of the plasma plume beyond the induction coil.

The combined trigger and charging and discharge circuits are shown in Fig. 2. The inner and outer diameters of the 3-turn planar induction coil (L_1) were 10 mm and 18 mm, respectively, and

the calculated inductance of the coil was 280 nH (L_1). The coil was made using a 1.1 mm diameter epoxy resin coated copper wire. The lumped inductance of the rest of the discharge circuit was 35 nH (L_2) while the total resistance of discharge circuit was 0.19 Ω (R_1), as determined from fitting the discharge characteristic curve (Fig. 3). The capacitor (C = 470 nF) was charged to 1.5 kV through a charging resistor R_2 = 2.2 kΩ. The discharge was switched using a VS-VSKT230-20PBF silicon-controlled rectifier (SCR) connected in parallel with an IXYS MDD95-12N1B diode (D). The discharge was switched, at a controllable delay after the laser pulse, using a DG 535 Stanford Digital Delay Generator (DDG). For a charging voltage of 1.5 kV, the amplitude of the first current maximum was ~1.1 kA, as determined by a Rogowski coil placed between the capacitor and the coil. The circuit was underdamped with a ringing period of ~2.2 μs.

Since the magnetic field produced by the induction coil is time varying, eddy currents are induced in a conducting target, which will tend to reduce the net magnetic field in the region of the induction coil. The reduction of the field can be minimized by moving the coil away from the target surface or reducing the area of the target. Simulations with COMSOL Multiphysics[20] were used to calculate B_z in the region of the coil, dependent on the target-coil separation. The
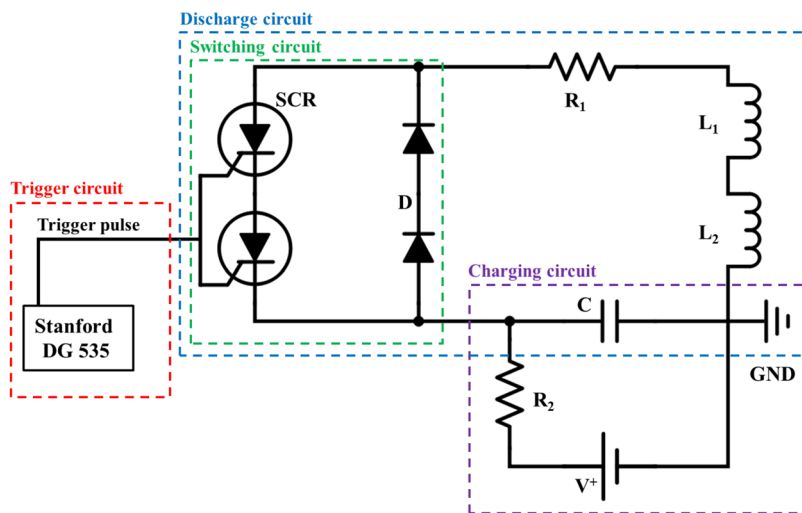
FIG. 2. Circuit schematic with the planar induction coil located at L_1. The circuit is divided into regions based on their primary function.

FIG. 3. (a) Color plot of B_z (T) in the x-z plane. The arrows indicate the field direction. (b) Plot of the variation of B_z along the z-axis ($x = y = 0$) for different target-coil separations. The calculation was done for a 1 mm thick, 20 mm square Cu target with a conductivity of $\sigma = 6 \times 10^7$ S m^{-1}.

FIG. 4. Plot of the temporal variation of the magnetic field at the coil center and the ion current density at the same position. Zero time corresponds to the laser pulse striking the target.

z-axis was taken as the coil axis and was normal to the target surface that lies in the x-y plane. The results shown in Fig. 4 are for a 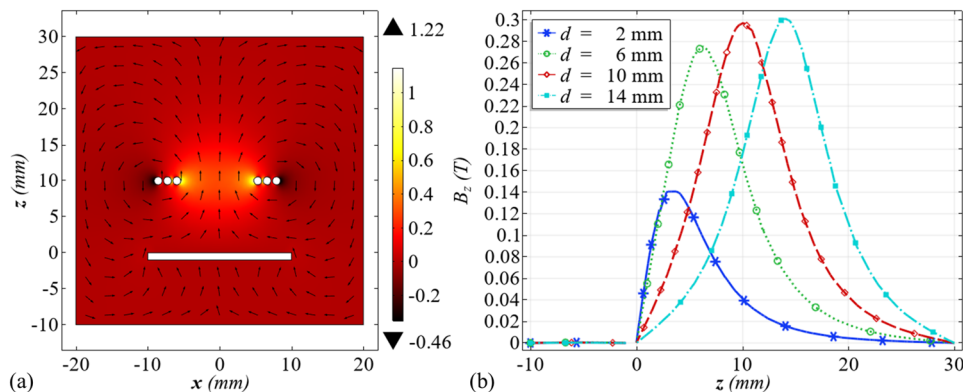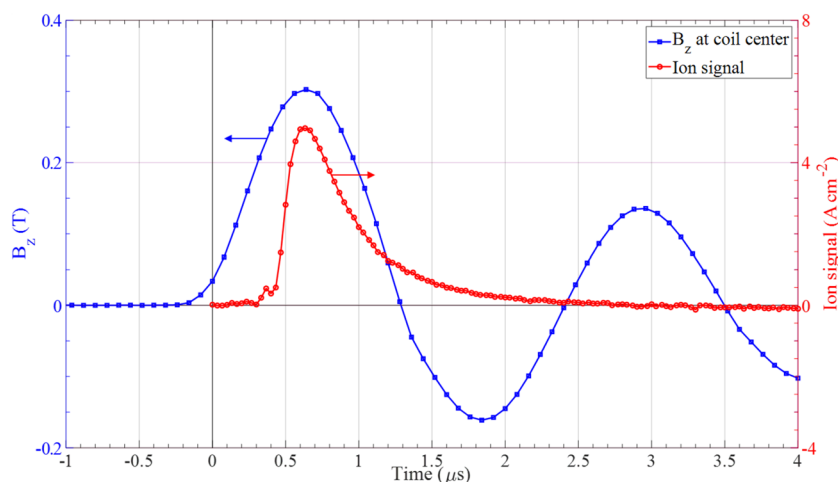1 mm thick, 20 mm × 20 mm square Cu target placed 10 mm from the coil. The electrical conductivity of copper was taken as $\sigma = 6 \times 10^7$ S m^{-1}. The current and frequency of the simulation was 1.1 kA and 455 kHz, respectively, following from the discharge characteristic (Fig. 4).

Figure 3(a) shows a color map of B_z in the x-z plane in the region of the coil. At the coil center $B_z = 0.3$ T, rising above 0.7 T near the edge of the central aperture. As expected, B_z falls to nearly zero near the surface of a highly conducting target, such as Cu. The red arrows indicate the direction of the magnetic field. Figure 3(b) shows plots of B_z along the coil axis for target-coil separations of $d = 2, 6, 10,$ and 14 mm. For d greater than ~10 mm, the reduction of the field at the coil due to eddy currents in the target is negligible.

The plasma heating and focusing depends on the relative timing of the arrival of the plasma pulse and the current waveform in the coil. The timing of the plasma pulse was determined by using a negatively biased Langmuir ion probe to measure the ion flux at 15 cm without excitation of the induction coil. Since the plasma flow is inertial, self-similar scaling can be used to determine the ion current density at the coil position (see Fig. 4). For the experiment described here, the peak ion current density at the coil coincides with the first maximum of the magnetic field (Fig. 4). The influence of discharge timing on the plasma heating and focusing has been described before[9,19] and is not discussed here.

Figure 5 is a timing diagram of the overall experimental setup. This diagram shows the spectrometer acquisition window (CAM 1), the imaging acquisition window (CAM 2), the DDG delay generator
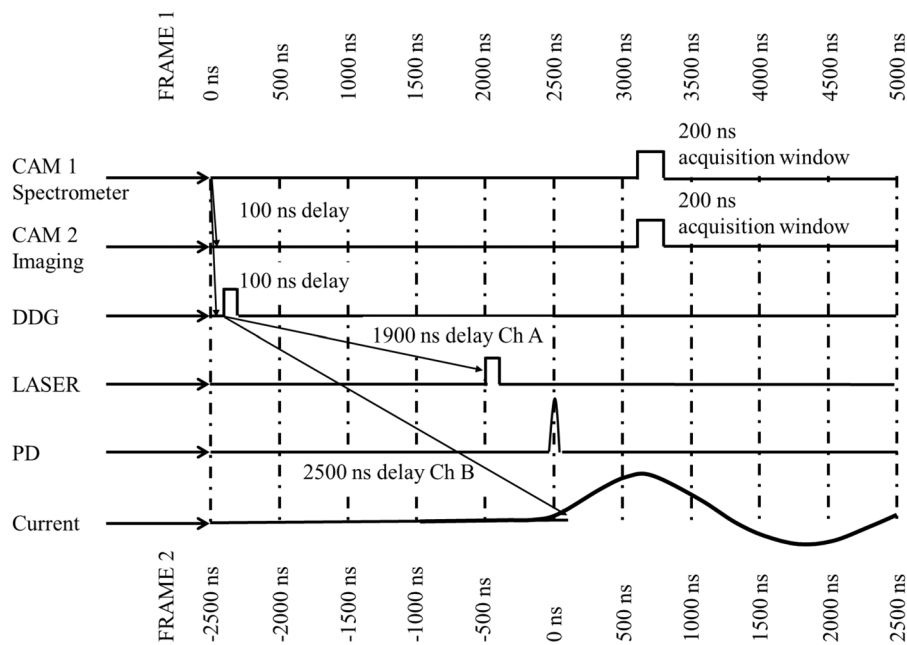

FIG. 5. Timing diagram for the discharge shown in Fig. 4 and also showing the 200 ns acquisition windows for the plasma imaging and spectroscopy.

laser initialization pulse, laser delay, laser photodiode response, and the current pulse through the SCR and discharge coil. The CAM1 feature consists of an ICCD camera (Andor USB iStar and Oriel MS260i spectrometer) and the CAM2 feature consists of an ICCD camera (Andor DH734) with spectral filters (listed below). The maximum timing jitter was approximately 20 ns for the whole setup. Frame 1 indicates the user frame while frame 2 represents the frame of the discharge with respect to the laser pulse hitting the surface of the target (t = 0 ns). In this setup, CAM1 has an in-built delay generator and was used to initiate the experiment and data acquisition. The sample timing sequence in Fig. 5 shows a 200 ns acquisition window from 600 to 800 ns after the laser pulse hits the target and when the coil current is at the maximum. This is achieved by the user initiating CAM 1 with a 3.2 μs delay. CAM 1 then triggers both CAM 2 and the DDG. The DDG then triggers the laser and coil current, and the arrival time of the laser pulse at the target is given by the PD signal.

Gated images of the plasma self-emission, up to 30 mm in front of the target, were acquired at a controllable delay after the laser pulse. Optical filters at 520 nm and 490 nm (FWHM = 10 nm) were used to record separately the observed line emission from Cu^0 and Cu^+. The acquisition time for these images was 200 ns. Time-resolved spectral emission measurements in the region 490–530 nm were made to investigate the influence of the magnetic field on the plasma temperature. These spectral measurements were absolutely calibrated, spatially resolved along the target normal, and synchronized to the image acquisition. To investigate how the plume flow beyond the coil is modified by the magnetic field, the laser ablated material transmitted through the coil aperture was deposited on microscope slides placed at varying distances from the coil. For these depositions, the target and coil were rotated by 45° with respect to the laser beam. This rotation elongated the laser ablation spot; thus, the laser energy was increased to maintain the fluence at 2 J cm^{-2}. The thickness distribution in the deposits was determined by measuring the film transmission at 515 nm using a calibrated flatbed scanner, as described by Donnelly et al.[21]

III. RESULTS

First, the time-resolved plasma imaging showed that excitation of the induction coil leads to strong enhancement of the UV/visible light emission, and this enhancement is strongly peaked when the rates of change of coil current, and thus plasma induced current, are maximum.[9] Figure 6 shows six side-on images of the plasma plume self-emission in a 30 mm × 30 mm region that includes the target and induction coil. The images were acquired over a 200 ns window starting at 1.2 μs after the laser pulse. Different color scales are used in each image, but the relative intensities can be directly compared. The obscuration of the image near 10 mm is due to the induction coil. The images in the left-hand column (a), (c), and (e) in Fig. 6 are for free ablation (B = 0). As expected, the coil aperture acted as a skimmer, obstructing the expansion of the periphery of the plume and transmitting a well-defined cone of plasma. At 1.4 μs, the visible plume extends to ~20 mm in front of the target, giving an expansion velocity consistent with the probe signal in Fig. 4(b). The images in Figs. 6(a) and 6(b) were recorded without a spectral filter and correspond to plasma emission across the spectral range of the ICCD (380–700 nm). There are several clear differences between

the field-off and the field-on images. In all regions, the emission is strongly increased; for example, just outside the coil, the increase is ×20. Comparatively, the plasma near the target is barely visible in the field-off case while it is the brightest region in the field-on case. It can also be noted that the plasma transmitted through the aperture appears to be converging to a focus at ~10 mm beyond the induction coil.

The images in Figs. 6(c) and 6(d) were recorded using the 520 nm band pass filter. Thus, these images are mainly due to the following neutral Cu spectral lines: $Cu^0\ 3d^{10}\ 4p\ ^2P_{1/2}-3d^{10}\ 4d\ ^2D_{3/2}$ at 515.32 nm and $Cu^0\ 3d^{10}\ 4p\ ^2P_{3/2}-3d^{10}\ 4d\ ^2D_{3/2,5/2}$ at 522.01 and 521.82 nm, respectively. The distribution of Cu line emission is quite similar to the broadband image. For the images in Figs. 6(e) and 6(f), a 490 nm filter was used, and the recorded emission is mainly due to the singly ionized copper lines: $Cu^+\ 3d^9\ 4d\ ^3G_5-3d^9\ 4f\ ^3H_6$ at 490.97 nm, $Cu^+\ 3d^9\ 4d\ ^3G_4-3d^9\ 4f\ ^1H_5$ at 493.16 nm, and $Cu^+\ 3d^9\ 4d\ ^1G_4-3d^9\ 4f\ ^3H_5$ at 495.37 nm. While Cu^+ line emission is barely visible in the field-off image [Fig. 6(e)], strong Cu^+ emission is observed in the region between the target and the coil, and in the focused plasma beyond the coil. These observations of magnetic induction in a LPP leading to increased light emission, a higher degree of ionization, and plasma focusing, can be explained within the framework of resistive magneto-hydrodynamics (MHD), as described in Creel et al.[9,19] The combined action of the changing magnetic flux from the coil and plasma flow across the magnetic field ($u \times B$) drives a current density j in the plasma. The induced currents cause plasma heating, and $j \times B$ forces lead to focusing of the plasma transmitted through the coil aperture.

Optical emission spectra in the 490–530 nm region, which are spatially resolved along the z-direction, are shown in Fig. 7, where in (a) the field is off and in (b) the field is on. These spectra were recorded over a 200 ns time interval starting at 1.2 μs after the laser pulse, as for the plasma images in Fig. 6. As before, the gap in emission at 10 mm from the target is due to obscuration of the plasma by the coil. The extent of the spectral lines in the z-direction agrees with the plasma imaging. Energizing the induction coil leads to a 3× increase of the intensity of the Cu^0 lines in the target-coil region and the appearance of strong Cu^+ lines both in the target-coil region and beyond the coil. These observations are consistent with spectral images in Fig. 6.

Since the spectrometer was absolutely calibrated and the plasma dimensions were measured, optical emission spectra can be analyzed to determine the plasma temperature and density. This was done using the spectral synthesis code PrismSPECT,[22] as previously reported.[9,19] It was noted that not all the observed Cu^0 and Cu^+ lines appear in the synthetic spectrum. This is due to the limitations of the atomic database used in PrismSPECT. For example, the strong Cu^0 line at 510.55 nm does not appear in the synthetic spectrum because the transition probability is set to zero in the code. Nevertheless, a sufficient number of lines are included to allow the spectral fits to be used for the determination of plasma temperature and density. For the field-off case, only three Cu^0 lines are observed [Figs. 7(a) and 8(a)], and they are not suitable for the determination of T_e using the line ratio method. However, if the atom/ion density in the plume is known, the absolute intensities of these lines can be used to find T_e. From the measurement of the total ion/atom number in the plume (see below), and using the Anisimov model of plume
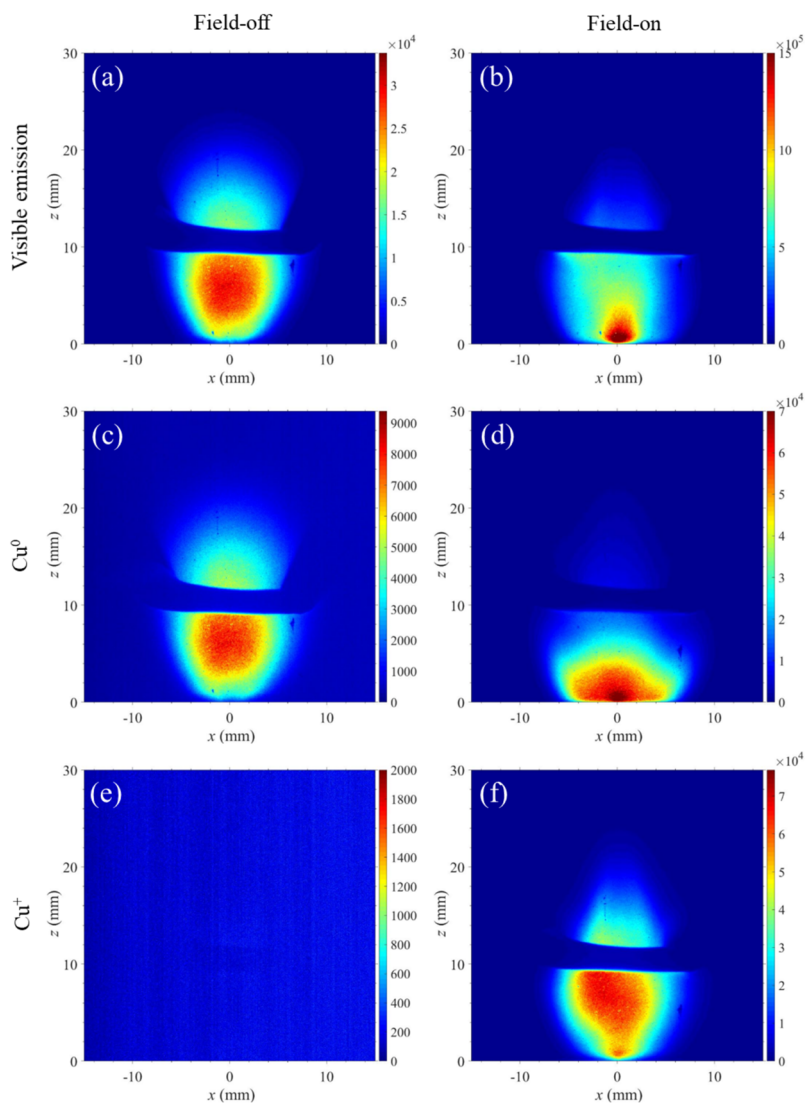
FIG. 6. Spectral imaging of the plasma plume with the field off [(a), (c), and (e)] and field on [(b), (d), and (f)] acquired over 200 ns starting at 1.2 μs.

expansion,[23] the atom/ion number density at 8.5 mm from the target was found to lie in the range $(3–10) \times 10^{13}$ cm^{-3}. Using this density, the spectrum in Fig. 8(a) was fitted using $T_e = 0.52 \pm 0.02$ eV, and the mean ionization is $Z = 0.1$. For the field-on case, the spectrum at 8.5 mm shows both Cu^0 and Cu$^+$ lines, and the ratio of these lines is very sensitive to temperature. Fitting the field-on spectrum from the 8 to 9 mm region gives $T_e = 1.7 \pm 0.1$ eV, an atom/ion density of $(6.2 \pm 0.3) \times 10^{13}$ cm^{-3}, and $Z = 1.8$. From the mean ionization values, it is estimated that the average energy per Cu ion/atom increases from ~1 eV in the free ablation to ~24 eV in the inductively heated plasma.

Head-on (along the z-axis) imaging provided very direct visual evidence of inductive heating taking place. Figure 9 shows four head-on images of the plume optical emission starting at 1100 ns and advancing in 20 ns steps to 1160 ns. It can be seen from Fig. 4 that in this time interval, the magnetic induction is maximal. A ring of enhanced optical emission at the periphery of the plasma is clearly

visible in the image at 1100 ns [Fig. 9(a)], which is due to inductive heating within the skin depth. At 1120 ns [Fig. 9(b)], ring brightness is increased. The image at 1140 ns [Fig. 9(c)] shows the ring of strong emission to be filling toward the center and nearly uniform emission is observed at 1160 ns [Fig. 9(d)]. The evolution of the spatial structure of inductive heating can be understood in terms of the diffusion of the imposed magnetic field into the plasma. The time interval for the magnetic field to diffuse to the center of the plasma column is given by is $\tau_p = \mu_0 \sigma R^2$, where σ is the plasma conductivity calculated using the Spitzer plasma resistivity formula[1] and R is the plasma radius determined from the ICCD imaging. Clearly in the time interval for acquiring the head-on images, the plasma temperature and conductivity are increasing. However, the field diffusion time can be estimated by fitting the emission spectrum to determine the plasma conditions in the interval 1000–1200 ns. There it was found that in the region 8–9 mm from the target, the plasma radius was ~6 mm and the temperature and density were 1.5 ± 0.1 eV and
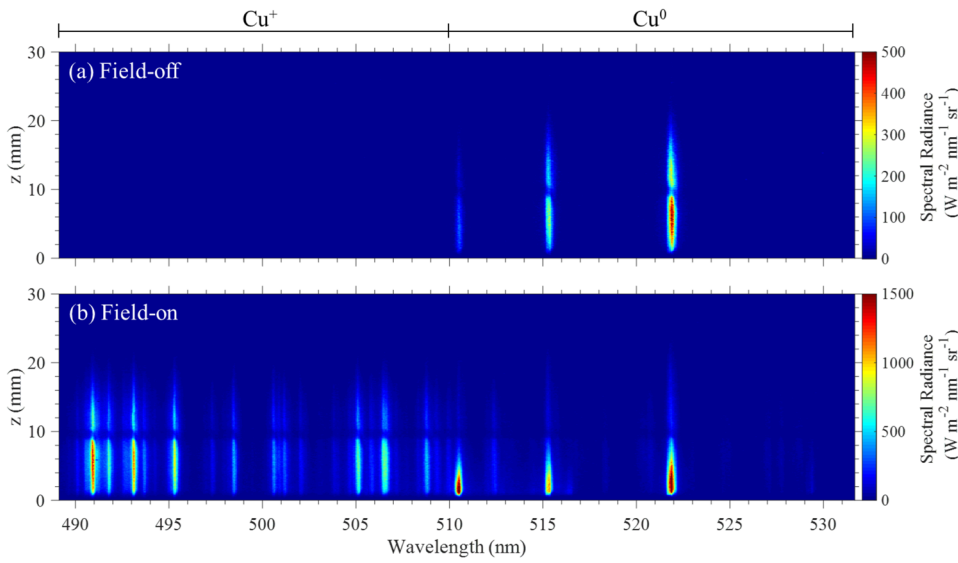
FIG. 7. Absolutely calibrated, space-resolved emission spectra of the plasma plume emitted in the time interval 1.2–1.4 μs after the laser pulse: (a) without the field and (b) with the field.
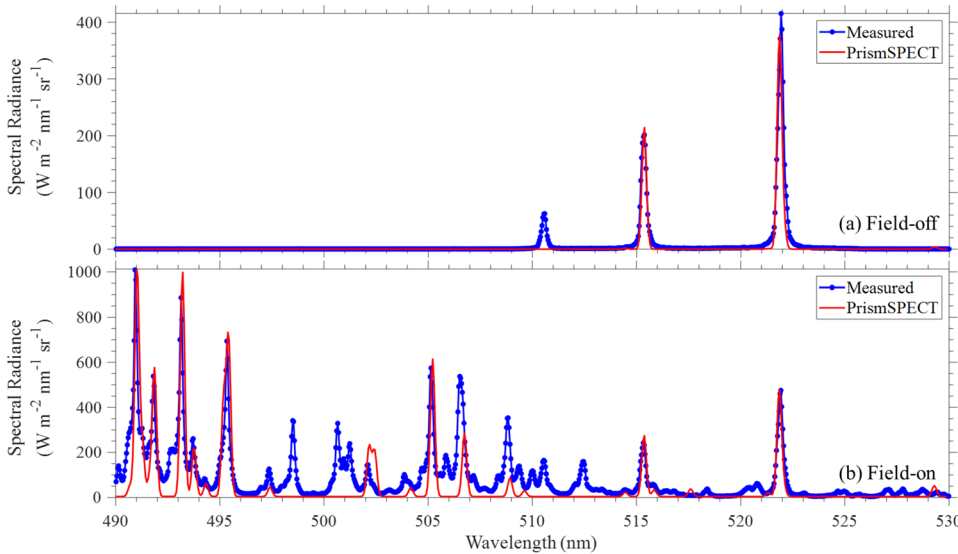

FIG. 8. Fitted spectra emitted from a region 8–9 mm from the target and in the interval 1200–1400 ns, for (a) the field-off case and (b) the field-on case.

$(4.5 \pm 0.4) \times 10^{13}$ cm^{-3}, respectively. For these plasma conditions, the conductivity is $\approx$1000 S m^{-1} and the time for the field to diffuse to the center is $\tau_P \sim 50$ ns, which is comparable to the value of 60 ns obtained from the head-on images.

As already noted, it was observed in Fig. 6(f) that the plasma transmitted through the aperture appears to be converging to a focus at ~10 mm beyond the induction coil. This aspect was investigated further by making Cu deposits on glass substrates at different positions beyond the coil and measuring the thickness distributions, and thence the deposition rate distributions, as shown in Fig. 10. The deposits in Figs. 10(a) and 10(c) were made without the magnetic field, and the substrate was placed at 12 mm and 20 mm from the target, respectively. The outer edge of the deposit is sharply defined by the skimming action of coil aperture, and the size of the deposit increases as the substrate is moved further away. Figures 10(b) and

10(d) show the deposition rate distributions for the field-on with substrates at 12 mm and 15 mm from the target. By making deposits with the pulsed magnetic field-on at 30 mm and 40 mm from the target (not shown here), it was observed that the size of the deposit has a minimum size at ~20 mm from the target, then diverges beyond that position.

For the field-off case, the peak deposition rate at the center of the deposit at 12 mm was 5×10^{-3} nm per shot, and the number of Cu atoms deposited per shot was 2.2×10^{13}, obtained by integrating the image of the deposition. By fitting the deposition profile to the equation describing the angular distribution of a laser ablation plume on a planar surface,[23,24] a value of ~7.5×10^{13} for the number of atoms in the ablation plume is obtained; this is close to the number of atoms ablated per pulse, as measured by mass loss. With the field on (Fig. 10), the size of the copper deposit
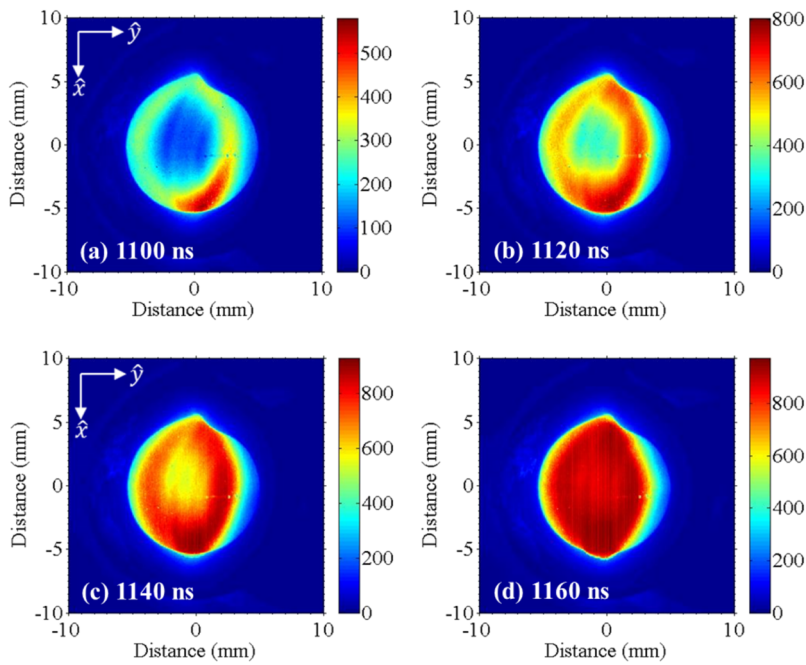
FIG. 9. Head-on 20 × 20 mm² images of the plasma plume showing a ring of enhanced emission in (a) and (b) due to inductive heating and filling of the ring in (c) and (d) as the imposed magnetic field diffuses to the plasma axis.
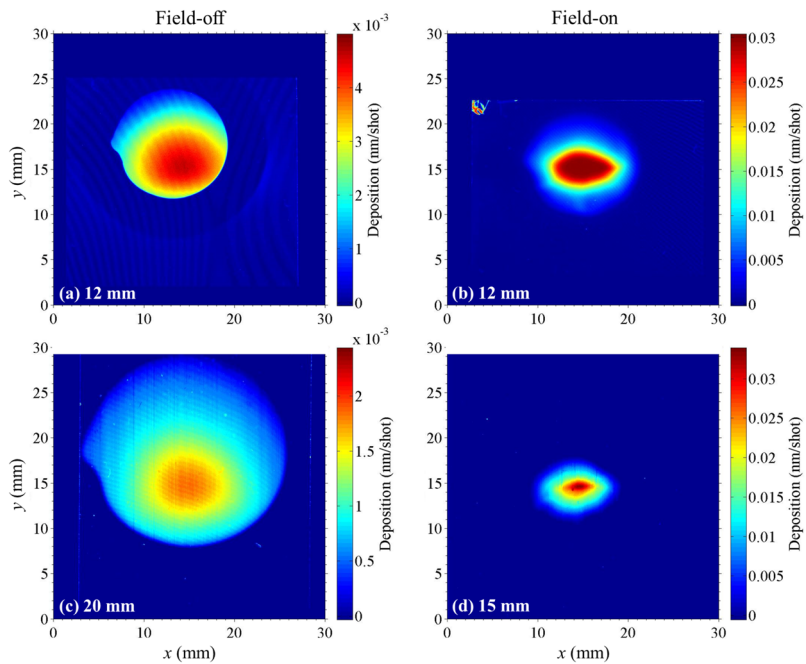

FIG. 10. Depositions of copper on glass substrates for [(a) and (c)] field-off and [(b) and (d)] field-on cases at 12 mm and 20/15 mm, respectively, from the target surface.

is much smaller and the maximum deposition rate increases to 3.5×10^{-2} nm per laser shot, ~7× higher than without the field. The total number of atoms deposited was 8.5×10^{13}. The reason for the noncircularity of field-on deposit is not yet clear but may be due to accuracy of the coil geometry. It can also be noted that, due to the rectangular beam spot on target, the ablation plume is not quite circular.

IV. CONCLUSIONS

A relatively simple pulsed magnetic induction coil was used as a noncontact method of on-the-fly heating of an LPP in vacuum in a region near the laser ablation target. Inductive heating leads to strong enhancement of the UV/visible spectral emission, and the degree of ionization is increased. Imaging of the plasma light

emission showed that the plasma transmitted through the central aperture of the induction coil is radially constricted and brought to a focus at ~10 mm from the coil. The plasma focusing was confirmed by making thin film depositions beyond the coil. It seems that this kind of device could find application in LIBS, PLD, and laser plasma ion sources.

ACKNOWLEDGMENTS

REFERENCES

[1] F. F. Chen, *Introduction to Plasma Physics* (Springer US, 1974), pp. 181, 183, 206.

[2] W. Neff, K. Bergmann, O. Rosier, R. Lebert, and L. Juschkin, Contrib. Plasma Phys. **41**, 589 (2001).

[3] M. A. Klosner and W. T. Silfvast, Opt. Lett. **23**, 1609 (1998).

[4] Y. V. Korobkin, I. V. Romanov, A. A. Rupasov, A. S. Shikanov, P. D. Gupta, R. A. Khan, S. R. Kumbhare, A. Moorti, and P. A. Naik, Laser Part. Beams **23**, 333 (2005).

[5] H. M. Smith and A. F. Turner, Appl. Opt. **4**, 147 (1965).

[6] R. Eason, *Pulsed Laser Deposition of Thin Films: Applications-Led Growth of Functional Materials*, 1st ed. (Wiley-Interscience, 2006).

[7] C. Pagano and J. G. Lunney, J. Phys. D: Appl. Phys. **43**, 305202 (2010).

[8] T. Kobayashi, H. Akiyoshi, and M. Tachiki, Appl. Surf. Sci. **197-198**, 294 (2002).

[9] J. R. Creel, T. Donnelly, and J. G. Lunney, Appl. Phys. Lett. **109**, 071104 (2016).

[10] R. Jordan, D. Cole, and J. G. Lunney, Appl. Surf. Sci. **109-110**, 403 (1997).

[11] C. Pagano, S. Hafeez, and J. G. Lunney, J. Phys. D: Appl. Phys. **42**, 155205 (2009).

[12] L. Dirnberger, P. E. Dyer, S. R. Farrar, and P. H. Key, Appl. Phys. A: Solids Surf. **59**, 311 (1994).

[13] C. de Julián Fernández, J. L. Vassent, and D. Givord, Appl. Surf. Sci. **138-139**, 150 (1999).

[14] S. S. Harilal, M. S. Tillack, B. O'Shay, C. V. Bindhu, and F. Najmabadi, Phys. Rev. E **69**, 026413 (2004).

[15] S. S. Harilal, B. O'Shay, M. S. Tillack, C. V. Bindhu, and F. Najmabadi, IEEE Trans. Plasma Sci. **33**, 474 (2005).

[16] A. Mostovych, B. Ripin, and J. Stamper, Phys. Rev. Lett. **62**(24), 2837–2840 (1989).

[17] K. J. Mason and J. M. Goldberg, Appl. Spectrosc. **45**, 1444 (1991).

[18] K. J. Mason and J. M. Goldberg, Appl. Spectrosc. **45**, 370 (1991).

[19] J. R. Creel and J. G. Lunney, Appl. Phys. A: Mater. Sci. Process. **124**, 124 (2018).

[20] See http://www.comsol.com/ for COMSOL v. 5.4a; accessed 2016.

[21] T. Donnelly, J. G. Lunney, S. Amoruso, R. Bruzzese, X. Wang, and X. Ni, J. Appl. Phys. **108**, 043309 (2010).

[22] See http://www.prism-cs.com/Software/PrismSPECT/overview.html/ for Prism-SPECT v4.7.0; accessed 2016.

[23] S. I. Anisimov, D. Bäuerle, and B. S. Luk'yanchuk, Phys. Rev. B **48**, 12076 (1993).

[24] S. I. Anisimov, B. S. Luk'yanchuk, and A. Luches, Appl. Surf. Sci. **96-98**, 24 (1996).